Title

Photoelectron Diffraction and Holography: Present Status and Future Prospects

Authors

Fadley, C.S.
Thevuthasan, S.
Kaduwela, A.P.
et al.

Publication Date

1993-08-01

LBL-35054
UC-404
Preprint

Lawrence Berkeley Laboratory
UNIVERSITY OF CALIFORNIA

Materials Sciences Division

Presented at the Fifth International Conference on Electron Spectroscopy, Kiev, Ukraine, July 26–August 1, 1993, and to be published in the Proceedings

Photoelectron Diffraction and Holography: Present Status and Future Prospects

C.S. Fadley, S. Thevuthasan, A.P. Kaduwela, C. Westphal, Y.J. Kim, R. Ynzunza, P. Len, E. Tober, F. Zhang, Z. Wang, S. Rubush, A. Budge, and M.A. Van Hove

July 1993

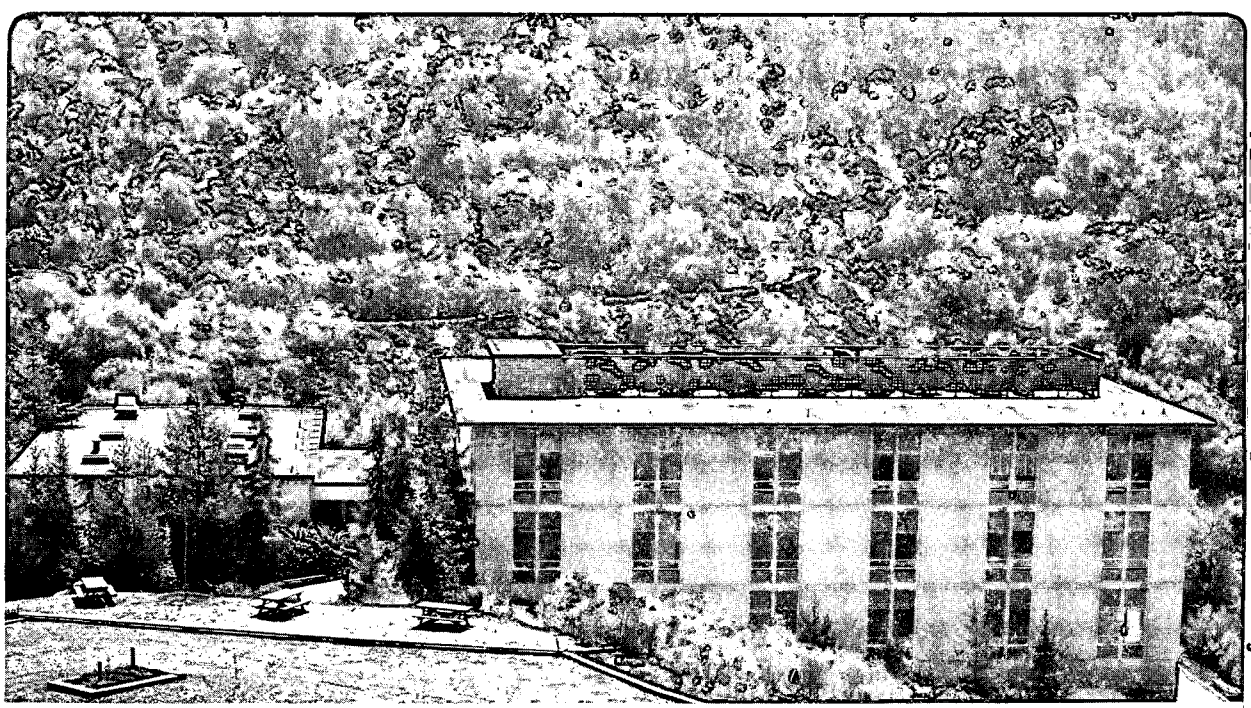

Prepared for the U.S. Department of Energy under Contract Number DE-AC03-76SF00098

DISCLAIMER

LBL-35054

PHOTOELECTRON DIFFRACTION AND HOLOGRAPHY: PRESENT STATUS AND FUTURE PROSPECTS

C.S. Fadley[#*], S. Thevuthasan[#], A.P. Kaduwela[*], C. Westphal[*], Y.J. Kim[@*], R. Ynzunza[#], P. Len[#], E. Tober[#*], F. Zhang[#], Z. Wang[#], S. Rubush[#], A. Budge[#], and M.A. Van Hove[*]

[*]Materials Sciences Division
Lawrence Berkeley Laboratory
University of California
Berkeley, California 94720

[#]University of California at Davis
Department of Physics
Davis, California 95616

[@]Department of Chemistry
University of Hawaii at Manoa
Honolulu, HI 96822

Acknowledgment

Work supported by the U.S. Department of Energy, Basic Energy Sciences, Materials Sciences Division under Contract DOE-AC03-SF00098 and the Office of Naval Research under Contract N00014-90-J-1457 and N00014-92-J-1140.

Invited paper to appear in The Proceedings of
The Fifth International Conference on Electron Spectroscopy
Kiev, Ukraine, August, 1993
(Journal of Electron Spectroscopy, in press)

PHOTOELECTRON DIFFRACTION AND HOLOGRAPHY: PRESENT STATUS AND FUTURE PROSPECTS[+]

C.S. Fadley[#*], S. Thevuthasan[#], A.P. Kaduwela[*], C. Westphal[*], Y.J. Kim[@#], R. Ynzunza[#], P. Len[#], E. Tober[#*], F. Zhang[#], Z. Wang[#*], S. Ruebush[#], A. Budge[#], and M.A. Van Hove[*]

[#]Department of Physics, University of California-Davis, Davis, CA 95616
[*]Materials Sciences Division, Lawrence Berkeley Laboratory, Berkeley, CA 94720
[@]Department of Chemistry, University of Hawaii-Manoa, Honolulu, HI 96822

ABSTRACT: Photoelectron diffraction and photoelectron holography, a newly developed variant of it, can provide a rich range of information concerning surface structure. These methods are sensitive to atomic type, chemical state, and spin state. The theoretical prediction of diffraction patterns is also well developed at both the single scattering and multiple scattering levels, and quantitative fits of experiment to theory can lead to structures with accuracies in the $\pm$0.03 Å range. Direct structural information can also be derived from forward scattering in scanned-angle measurements at higher energies, from path length differences contained in scanned-energy data at lower energies, and from holographic inversions of data sets spanning some region in angle and energy space. Diffraction can also affect average photoelectron emission depths. Circular dichroism in core-level emission can be fruitfully interpreted in terms of photoelectron diffraction theory, as can measurements with spin-resolved core-spectra, and studies of surface magnetic structures and phase transitions should be possible with these methods. Synchrotron radiation is a key element of fully utilizing these techniques.

INTRODUCTION

Photoelectrons emitted from core levels represent localized sources of outgoing waves which can then scatter from nearby atoms to produce diffraction patterns, and such diffraction patterns can be used to determine surface structures [1-5]. We will here consider several new directions for using such diffraction patterns to determine surface atomic positions, as well as surface magnetic structures. The analysis of such data in a more recently suggested holographic manner [6,7] so as to directly image atoms in three dimensions will also be discussed.

PHOTOELECTRON DIFFRACTION--BASIC CONCEPTS

Photoelectron diffraction patterns are by now well known and much studied, and have lead to the increasing use of this technique for surface structure studies [1-39]. The fundamental measurement is illustrated in Fig. 1(a). A photoelectron is emitted from a core level, and its intensity is measured as a function of its direction or its energy above a single-crystal sample, yielding what can be termed scanned-angle or scanned-energy data, respectively. In terms of the electron wave vector $\underline{k}$, this is equivalent to measuring intensity as a function of its direction $\hat{k} = \underline{k}/|\underline{k}|$ or its magnitude $k = |\underline{k}|$. Intensity variations are produced

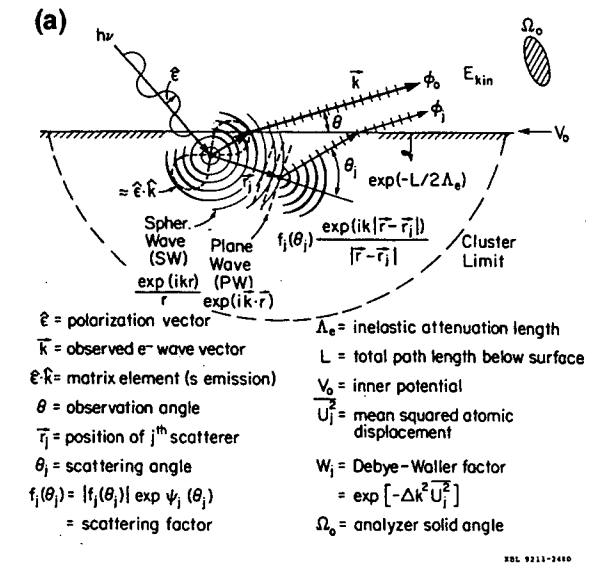

(b) Ge(111) - Ge 3d Photoelectron Hologram

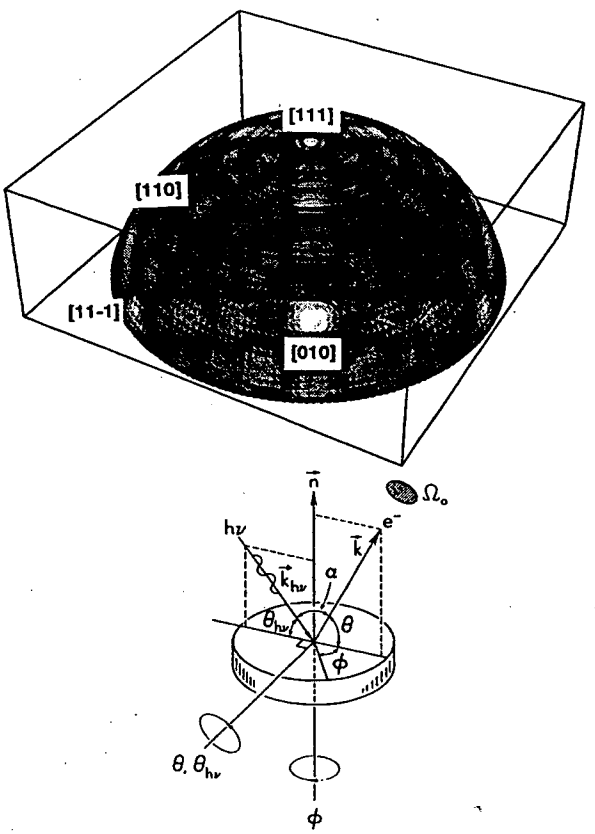

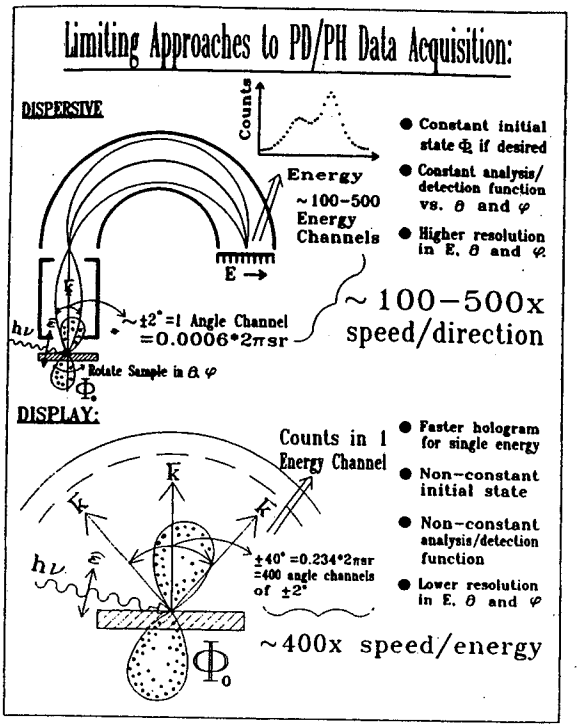

Fig. 2- Schematic comparison of the two limiting approaches presently available for obtaining photoelectron diffraction and holography data: an energy-dispersive analyzer and a display analyzer. Various parameters, as well as advantages and disadvantages, are indicated.

Fig. 1- (a) The basic process involved in photoelectron diffraction, with important physical variables indicated. Only single scattering is indicated for simplicity. In a holographic interpretation of such measurements, the direct or unscattered wave ϕ_o is identified with the reference wave, and the scattered waves ϕ_j are identified with object(subject) waves. (b) A schematic of the experiment, with an experimental diffraction pattern (hologram) for Ge 3d emission from Ge(111) [from ref. 23b] shown above the specimen.

by the interference of the unscattered or direct wave component ϕ_o and the various scattered-wave components ϕ_j. In Fig. 1(b) is shown a schematic experimental geometry, in which an actual experimental intensity distribution for Ge 3d emission from Ge(111) [23b] is plotted on a hemisphere above the specimen.

The resulting photoelectron intensity as a function of wave vector can be written in a simple single scattering picture as [1b-d]:

$$I(\underline{k}) \propto |\phi_o + \Sigma_j \phi_j|^2$$

$$\propto |\phi_o|^2 + \Sigma_j(\phi_o^* \phi_j + \phi_o \phi_j^*) + \Sigma_j \Sigma_k \phi_j \phi_k^* \ , \qquad (1)$$

where ϕ_j and ϕ_k are arbitrary scattered waves. For the illustrative case of photoelectron emission from an s subshell into an outgoing ϕ_o with p character, the individual wave components here can be written out more explicitly in terms of (cf. Fig. 1(a)): dipole matrix elements that are for <u>linearly polarized</u> radiation proportional to the dot product of the polarization direction ($\hat{\epsilon}$) and the relevant emission direction ($\hat{k}$ or $\underline{r}_j/r_j = \hat{r}_j$); inelastic exponential decay factors $\exp(-L/2\Lambda_e)$, with L equal to the total length for some path below the surface and Λ_e equal to the inelastic attenuation length for photoelectron <u>intensity</u>; scattering factors $f_j(\theta_j, r_j)$ involving both an amplitude $|f_j(\theta_j, r_j)|$ and a phase shift $\Psi_j(\theta_j, r_j)$ that are functions of the scattering angle θ_j, and, in more accurate spherical-wave scattering, also of the distance r_j to a given scatterer; Debye-Waller factors W_j that allow for attenuation of interference due to vibrational effects; and finally, phase shifts due to path length differences of the form $\exp[ikr_j]\exp[-i\underline{k}\cdot\underline{r}_j] = \exp[ikr_j(1-\cos\theta_j)]$. All structural information is contained in this last exponential factor, with the path length difference between ϕ_o and ϕ_j being given by $r_j(1-\cos\theta_j)$. Eq. 1 thus can be rewritten as:

$$I(\underline{k}) \propto |(\hat{\epsilon}\cdot\hat{k})\exp(-L_o/2\Lambda_e) + \Sigma_j(\hat{\epsilon}\cdot\hat{r}_j/r_j)|f_j(\theta_j, r_j)|W_j \cdot\exp(-L_j/2\Lambda_e)\exp[i\{kr_j(1-\cos\theta_j)+\Psi_j(\theta_j, r_j)\}]|^2 \ , \qquad (2)$$

or, in more convenient notation:

$$I(\underline{k}) \propto |F_o + \Sigma_j F_j \exp[-i\underline{k}\cdot\underline{r}_j]|^2 \ , \qquad (3a)$$

with

$$F_o(\underline{k}) = (\hat{\epsilon}\cdot\hat{k})\exp(-L_o/2\Lambda_e) \qquad (3b)$$

$$F_j(\underline{k}, \underline{r}_j) = (\hat{\epsilon}\cdot\hat{r}_j/r_j)|f_j(\theta_j, r_j)|W_j \cdot\exp(-L_j/2\Lambda_e)\exp[ikr_j] \cdot\exp[i\Psi_j(\theta_j, r_j)] \ . \qquad (3c)$$

Eqs. 3 can also be formally generalized to include multiple scattering [7a,8d], in which case each F_j must involve a sum over the various single and multiple scattering pathways m with different total lengths L_{mj} that terminate in scatterer j just before going to the detector. For emission from a subshell other than s (i.e. for $l_{initial} > 0$),

the above expressions become more complex due to sums over initial and final magnetic quantum numbers and interference between the two final-state channels $l_{final} = l+1$ and $l-1$ that are allowed by the dipole selection rules [8a,8d,9].

Expanding the square in Eq. 3a now yields

$$I(\underline{k}) \propto |F_o|^2 + \Sigma_j[F_o^* F_j \exp\{-i\underline{k}\cdot\underline{r}_j\} + F_o F_j^* \exp\{i\underline{k}\cdot\underline{r}_j\}] + \Sigma_j\Sigma_k[F_j^* F_k \exp\{i\underline{k}\cdot(\underline{r}_j-\underline{r}_k)\} + F_j F_k^* \exp\{-i\underline{k}\cdot(\underline{r}_j-\underline{r}_k)\}] \quad (4)$$

$|F_o|^2$ is thus simply proportional to $I_o(\underline{k})$, the intensity in the absence of any scattering. A normalized intensity function $\chi(\underline{k})$ can now be calculated, very much as in the analysis of extended x-ray absorption fine structure (EXAFS), with one choice being [7a]:

$$\chi(\underline{k}) = [I(\underline{k}) - I_o(\underline{k})]/I_o(\underline{k})^{1/2} , \quad (5)$$

and this yields

$$\chi(\underline{k}) \propto (|F_o|)^{-1}\Sigma_j [F_o(\underline{k})^* F_j(\underline{k}) \exp\{-i\underline{k}\cdot\underline{r}_j\} + F_o(\underline{k}) F_j(\underline{k})^* \exp\{i\underline{k}\cdot\underline{r}_j\}] + (|F_o|)^{-1}\Sigma_j\Sigma_k [F_j(\underline{k})^* F_k(\underline{k}) \exp\{i\underline{k}\cdot(\underline{r}_j-\underline{r}_k)\} + F_j(\underline{k}) F_k(\underline{k})^* \exp\{-i\underline{k}\cdot(\underline{r}_j-\underline{r}_k)\}]. \quad (6)$$

This form is useful in considering holographic analyses of diffraction.

Another common approximation is to assume that the scattered waves ϕ_j and ϕ_k are small in amplitude with respect to ϕ_o, so that the cross terms $\phi_o^* \phi_j$ and $\phi_o \phi_j^*$ in Eq. 1 dominate the structural information. This leads via Eqs. 3 and 6 to

$$\chi(\underline{k}) \propto 2\Sigma_j(\hat{\epsilon}\cdot\hat{r}_j/r_j)|f_j(\theta_j)|W_j \cdot\exp(-L_j/2\Lambda_e) \cdot\cos[kr_j(1-\cos\theta_j)+\Psi_j(\theta_j,r_j)] . \quad (7)$$

This form directly shows that Fourier transforms of scanned-energy data along some direction $\hat{k}$ and over some interval Δk

$$F_{\Delta k}(\hat{k},r) \propto \int_{\Delta k} \chi(\underline{k})\exp[-ikr]dk \quad (8)$$

should be useful for deriving path length differences $r = r_j(1-\cos\theta_j)$, a result that was first pointed out some time ago [10] and has been used in a number of subsequent studies [4,5,24].

There are several important characteristics of such photoelectron diffraction patterns:

-Measurement of intensities: In general, core peak intensities must be measured by accumulating data for the full spectrum and then accurately allowing for the inelastically-scattered background on which the elastic intensity rides. At a minimum, one must accumulate three energy points above, on, and below the peak to make this background correction. The low-energy background is known to exhibit diffraction features

that can be much different from those of the elastic intensity [11], and the high-energy background is in general due to secondary electrons from other photoelectron or Auger peaks that may exhibit different diffraction patterns. Therefore, ignoring the background correction as suggested recently [12] could introduce significant errors in the diffraction pattern and is not expected to be a generally reliable method.

There are two limiting approaches for measuring such photoelectron diffraction patterns in an efficient way, as illustrated in Fig. 2. An energy-dispersive analyzer can be used with multichannel detection to accumulate a full spectrum of interest along one direction of emission at one time [1-5], with the specimen being rotated under the analyzer so as to vary emission direction. Or, a display-type analyzer can be used to measure the intensity in a small energy interval over a number of emission directions [4c,31]. As indicated in this figure, both of these approaches have certain advantages. The dispersive analyzer should in general yield higher resolutions in both energy and direction if desired. The display analyzer on the other hand should permit acquiring data more quickly over a large solid angle. The dispersive analyzer looks at the same direction in the differential cross section responsible for creating ϕ_o as the sample is rotated under it, whereas there are variations in this cross section, and perhaps also selection rules connected with it, over the image in the display analyzer. The image in the display analyzer also may be distorted and/or modulated by non-uniform detection efficiencies that are not present in the dispersive analyzer. Both types can in principle lead to gains of 100-500x in data acquisition speed if one considers the number of energy channels or directions (here normalized to a typical angular resolution of $\pm 2°$) detected simultaneously. Thus, photoelectron diffraction measurements can be carried out fruitfully in either of these limits, with one or the other perhaps being preferred depending on the precise problem under study.

-Atom specificity: Photoelectron diffraction is inherently atom-specific, since core level energies can always be found that are unique to a given atom. Thus, the local structure around each of the atomic types in a sample can be studied, and this is a key advantage compared to many other structural probes [1b].

-Chemical-state specificity: For many systems, core levels furthermore exhibit chemical shifts or surface shifts, so that the structure around different chemical/surface states of the same atom can in principle be studied separately. This has been applied for example to distinguishing surface and bulk metal atoms [13a], the different sites in adsorbed molecules [13b] or atoms [13c], and different layers near epitaxial interfaces and surfaces [13d]. This application often requires energy resolutions in the 0.1-0.3 eV range, and is thus well-suited to synchrotron radiation studies.

-Spin specificity: In atoms or

molecules with a net magnetic moment, exchange-produced splittings of core levels in which the spin-up and spin-down photoelectrons are separated in energy can also arise [14a]. The degree of spin polarization in such multiplet peaks is defined by $P = [I(\uparrow)-I(\downarrow)]/[I(\uparrow)+I(\downarrow)]$, with $I(\uparrow)$ and $I(\downarrow)$ equal to the spin-up and spin-down intensities, respectively. Multiplet polarizations are internally-referenced to the orientation of the emitting magnetic moment [14b-e]. If on the other hand circularly polarized radiation is used to excite spin-orbit-split core levels, a significant degree of spin polarization (now externally-referenced to the direction of incidence of the light) can be induced in the outgoing photoelectrons [15]. Such measurements require synchrotron radiation, as discussed further below. Finally, an externally-referenced spin detector can be used to directly measure the spin polarization over a given core spectrum [16]. These ways of inducing or measuring spin selectivity suggest the use of spin polarized photoelectron diffraction in the study of magnetic materials, as amplified below. In order to enhance magnetic scattering effects, kinetic energies of approximately 100 eV are required [14b], thus again in general implying synchrotron radiation for excitation.

-Well-defined and controllable emission process: Although similar short-range-order diffraction is found in Auger electron emission [1,2], the electron excitation of Auger processes [17], quasi-elastic back-scattered Kikuchi electrons [1c,2a,18], and diffuse LEED and fractional-order LEED [19], the physics of the emission process is best understood for photoelectron emission. That is, the initial core level is described by a given l value, and the dipole excitation leads to only two interfering channels of $l \pm 1$. Thus, theoretical modeling can be the most accurate for photoelectron diffraction and holography. Varying both the polarization and energy of the exciting photon also can be used to emphasize different scatterers or aspects of the emission or scattering process.

-Simple forward scattering: In measurements at photoelectron kinetic energies of about 500 eV or higher, the scattering amplitude $|f_j(\theta_j,r_j)|$ is highly peaked in the forward direction (i.e. near $\theta_j = 0$). Many studies have by now shown that such forward scattering or forward focussing peaks can be directly used to determine bond directions for adsorbed molecules [1,3] and low-index directions for single crystals and epitaxial overlayers [1,2]. As an illustration of the sensitivity of such high-energy patterns to different surface structures, Fig. 3 shows the full 2π intensity distributions above three different surfaces, in stereographic projection [2c]: fcc Ni(001) [20], hcp Ru(0001) [21], and the textured surface of highly oriented pyrolytic graphite with a preferred (0001) orientation [22]. Osterwalder et al. [2c] have been particularly effective in using such 2π distributions in the study of surface structures and epitaxial growth. The intensities of the dominant forward scattering peaks in such intensity distributions have also been found

Ni(001):Ni 2p at 636 eV

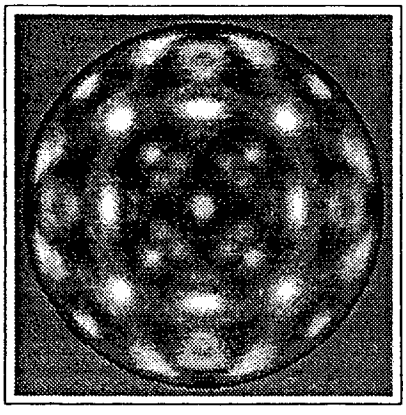

Ru(0001):Ru 3d at 1206 eV

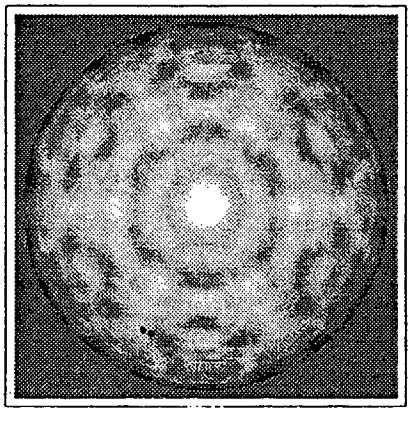

Graphite (0001): C 1s at 946 eV

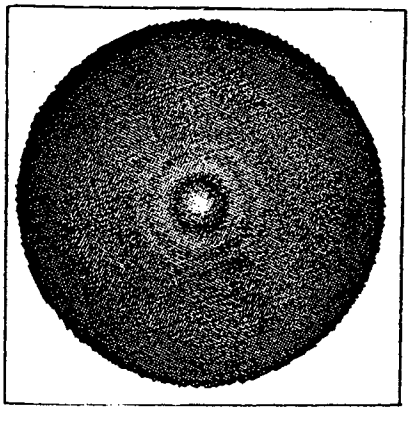

Fig. 3- Full 2π XPS intensity distributions from several surfaces: fcc Ni(001) [20], hcp Ru(0001) [21], and highly oriented pyrolytic graphite [22].

to be sensitive to surface premelting phenomena [23]. The higher kinetic energies required for this kind of measurement have led to its being performed primarily with laboratory x-ray sources in the 1.2-1.5 keV range, but higher brightness synchrotron radiation sources in the 500-1500 eV range should be equally useful for this work.

- Back scattering: In measurements at lower photoelectron kinetic energies of less than about 300 eV, there is also a significant degree of back scattering, and this can be used in several ways to extract structural information concerning atoms that are "behind" the emitter as viewed by the detector [1,4,5,10,24]. Synchrotron radiation is again necessary to insure sufficiently low kinetic energies in such studies.

- Single scattering and multiple scattering analysis: In a number of prior studies, it has been found that a simple single scattering model such as that outlined above is able to predict most of the structure in diffraction patterns, and thus it also can be useful for deriving some structural information. However, multiple scattering effects can be strong in both forward scattering along high-density rows of atoms (where events of order up to the number of scatterers between emitter and scatterer may have to be considered [8d]) and back scattering at lower energies (where events up to third order are found to be essential for predicting all diffraction features [8d,e]). The forward scattering case is illustrated in Fig. 4, where experimental and

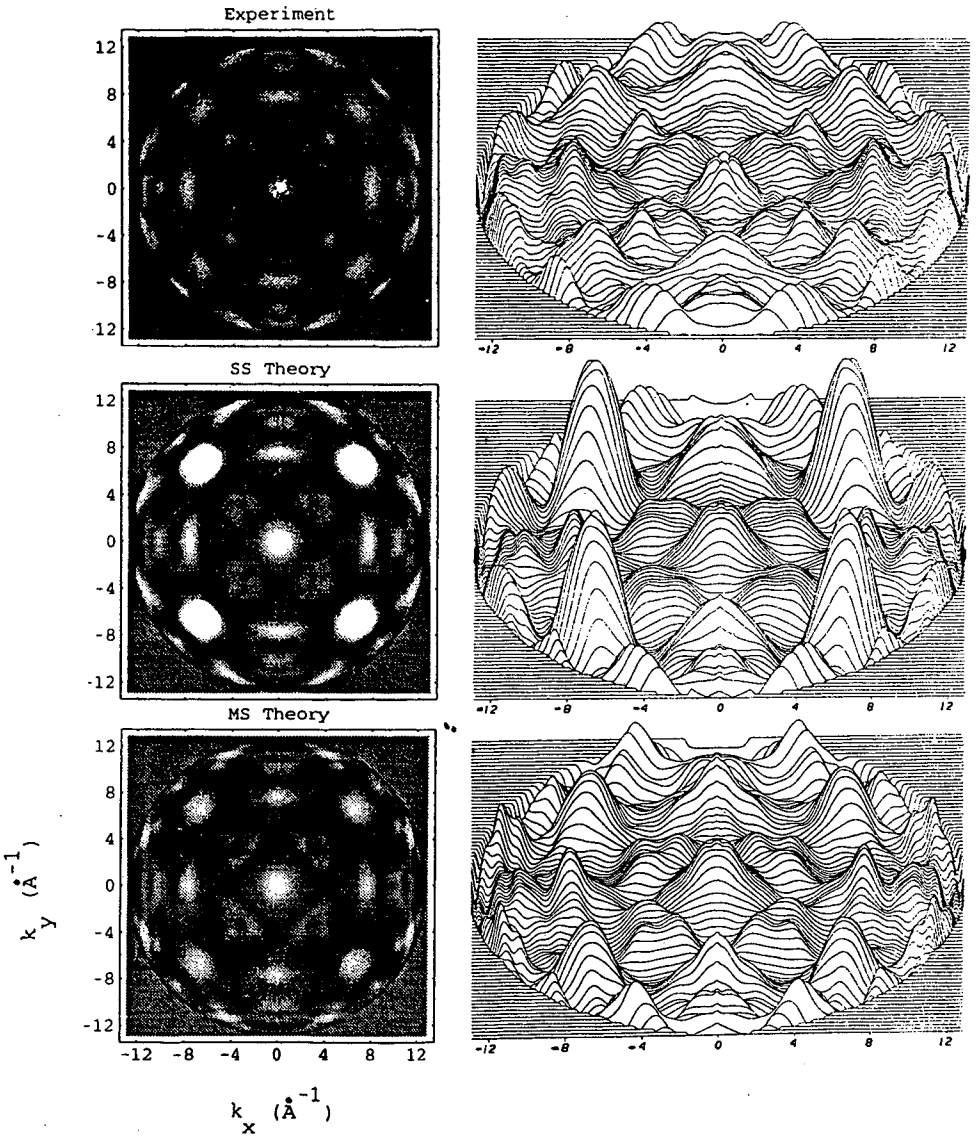

Fig. 4- The Ni $2p_{3/2}$ intensity above a Ni(001) surface as excited by Al Kα radiation, shown in two different representations: experimental data are compared with single scattering theory and multiple scattering theory. [From Thevuthasan et al., ref. 20]

calculated full diffraction patterns above a Ni(001) surface are shown [20], here projected down onto the k_x-k_y plane, with k_z along the surface normal. The experimental pattern away from low-index directions is well predicted by single scattering theory, but both the intensity and width of the low-index forward scattering peaks are much overestimated in this simple model. Multiple scattering theory by contrast predicts all aspects of the diffraction pattern very well, even though only five emitter layers were included in this simulation. Multiple scattering reduces the intensities and widths along low-index directions due to what have been termed "defocussing" effects [8d,25].

- Influence of diffraction on electron escape depths: We consider now the influence of single and multiple elastic scattering on the important question of average escape depths in higher-energy XPS studies on single crystals, as studied recently by Ynzunza et al. [26]. Fig. 5 shows some theoretical calculations of these effects for the simple case of electron emission at 636 eV from linear chains of Ni atoms with the bulk [001] spacing of a = 3.52 Å, embedded in an isotropic medium with a typical inelastic attenuation length of 9.8 Å. The chain length is varied to simulate Ni layers of varying thicknesses, but emission is allowed from every atom j in a given chain, as would be measured experimentally. If the intensity from the jth atom in a given direction is $I_j(\hat{k})$ and the atomic spacing along the chain is a, then the average depth of emission can be calculated from:

$$\bar{Z}(\hat{k}) = \Sigma_j(ja)I_j(\hat{k})/\Sigma_j I_j(\hat{k}). \qquad (9)$$

The curves here all show local maxima along the chain direction due to forward scattering. Those in multiple scattering are less pronounced due to defocussing effects, but still present. There are also maxima at about $\pm 28°$ and $\pm 40°$ that are due to 1st-order and 2nd-order constructive interferences, respectively [1]. However, between these maxima are pronounced decreases in $\bar{Z}(\hat{k})$ due to destructive interference effects which attenuate the intensities of atoms away from the surface. Thus, it is predicted that, due to elastic scattering and diffraction, the average depth of emission in XPS above a single crystal can vary by as much as 30% with direction, being lower just adjacent to the lowest-index directions. Calculations for clusters with more atoms and overlapping diffraction from several atomic rows smear these effects out somewhat, but still reveal variations of as much as 20-30% [26]. Quantitative analyses of XPS spectra thus should take into account such effects on average sensing depths.

-Path-length differences: Another direct form of structural information that can be obtained by virtue of the strong single scattering character of photoelectron diffraction is the path length difference associated with a given scatterer j: $r_j(1-\cos\theta_j)$ [1,4,5,10,24]. As noted in connection with Eq. 8, this requires Fourier transforming scanned-energy data over some interval Δk, and in turn implies

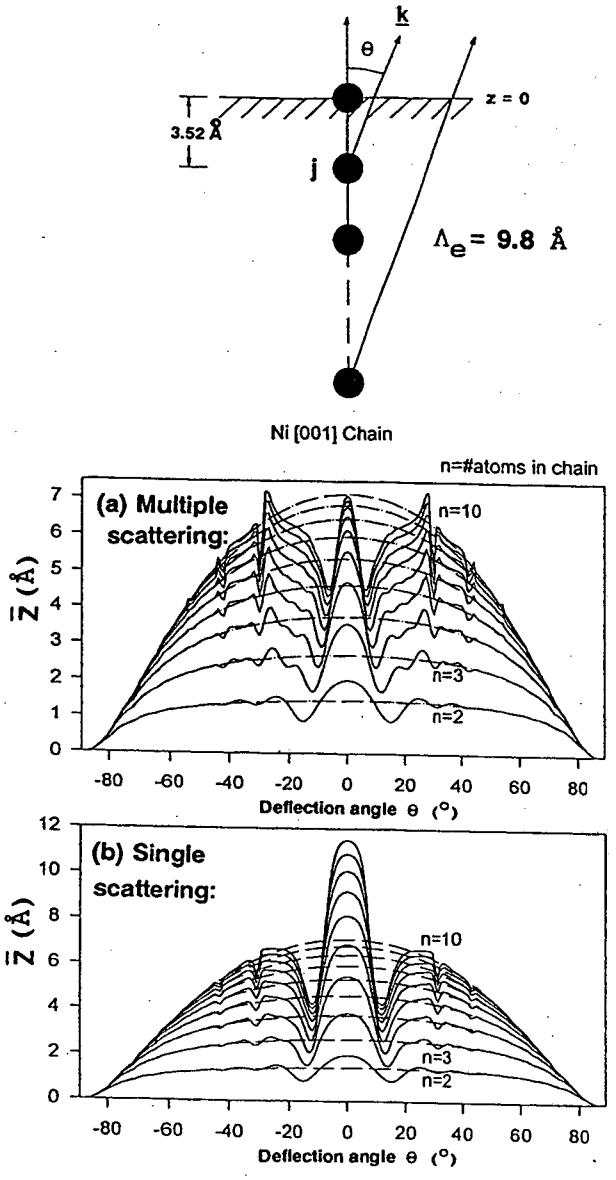

Fig. 5- The calculated variation in average emission depth as a function of direction $\bar{z}(\hat{k})$ from a [100] chain of Ni atoms of different lengths for emission at an energy of 636 eV. θ is the angle of deflection away from the chain axis. (a) shows multiple scattering calculations, and (b) corresponding single scattering calculations. The dashes curves represent the effects of isotropic inelastic scattering alone. [From Ynzunza et al. ref. 26]

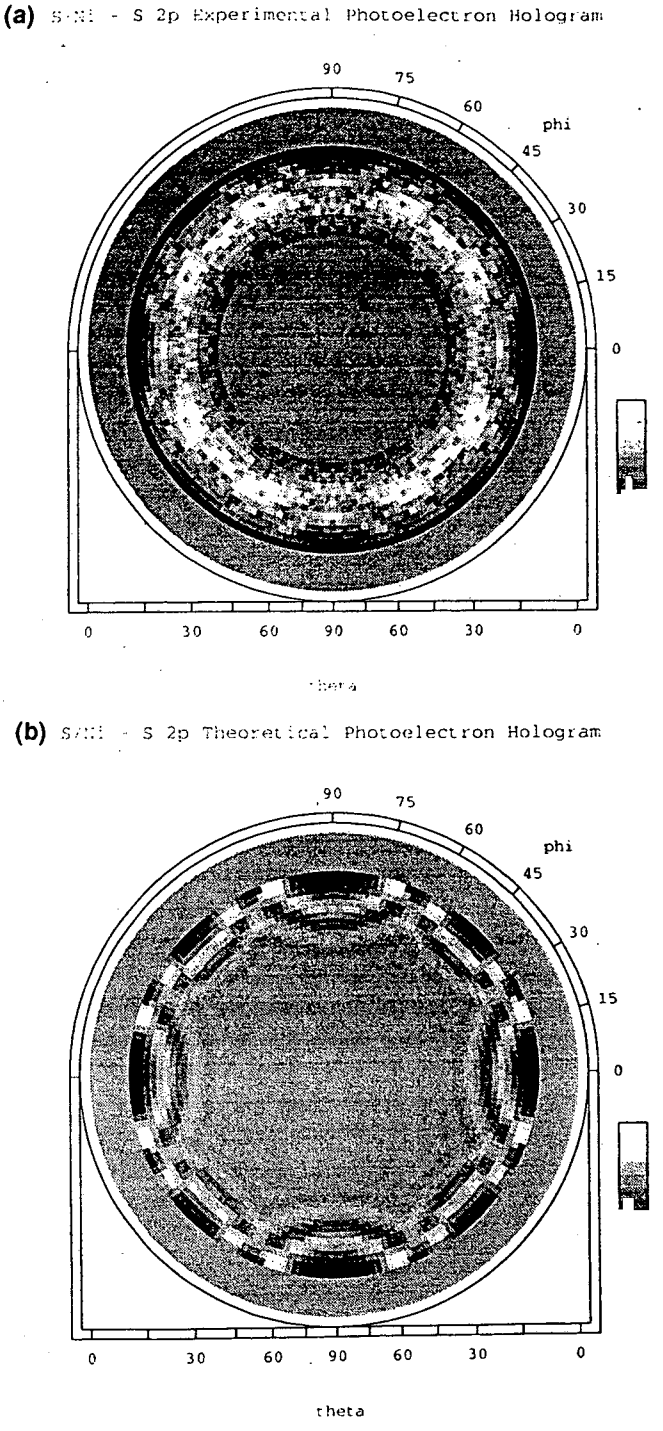

Fig. 6- (a) Experimental and (b) single-scattering theoretical S 2p diffraction patterns at 1324 eV from a c(2x2)S overlayer on Ni(001). The data extend from 10° to 40° above the surface. [From Thevuthasan et al., ref. 29c]

the use of synchrotron radiation so as to be able to vary energy (and thus k) in small steps. The presence of the scattering phase shift $\Psi_j(\theta_j,r_j)$ in Eq. 7 also can lead to errors in path length differences derived in this way, unless a correction is somehow made for it in doing the transform [10]. However, Shirley et al. [4c] have recently found highly accurate path length differences by using Eq. 8 without phase shift corrections for properly chosen adsorbate experimental geometries. Two other variations in the use of Eq. 8 have recently been proposed by Fritzsche and Woodruff [24a] and by Hofmann and Schindler [24b] as methods of making first estimates of nearest-neighbor positions relative to an adsorbate [24].

-Accurate surface structures: In a growing number of studies to date, it has been possible also to determine more detailed surface structures by fitting experimental diffraction patterns of either the scanned-angle or scanned-energy type to theoretical simulations for various possible trial geometries [1,2a,4,5,8b,8d]. Direct structural information from forward scattering or back-scattering path length differences can often be used to eliminate various possible structures and arrive at a very good initial guess for the final trial-and-error search. Theoretical calculations have been carried out at both the single scattering [1,2a] and more accurate multiple scattering [1,4,5,8] levels. With careful analysis of such fits, e.g., via R factors, accuracies in the approximately $\pm$0.03Å range have been obtained. However, further work is needed to speed up such structure searches and the multiple scattering calculations needed for the highest ultimate accuracy. Finally, more rapid data acquisition methods are also called for; these will benefit from next-generation higher-brightness synchrotron sources as well.

PHOTOELECTRON HOLOGRAPHY

More recently, it has been suggested by Szöke [6] that such photoelectron diffraction patterns can be treated as holograms, with the unscattered wave ϕ_o being identified as the reference wave of the hologram, and the scattered waves ϕ_j being identified as the object waves. A diffraction pattern that is somehow measured over a relatively large number of points in $\underline{k}$ space which may involve varying both direction and energy is then converted into a direct three-dimensional image of the atoms surrounding a given atom using a Fourier-transform-like integral. The hologram is in this interpretation just the intensity $I(\underline{k})$, or more conveniently the normalized function $\chi(\underline{k})$. The holographic analysis of diffraction data is in a much more developmental stage, but several encouraging experimental studies have been carried out to date [4c,12,28-33].

The first holographic imaging procedure to be demonstrated quantitatively is due to Barton [7a]. It makes use of scanned-angle data at a single energy, for which the Helmholtz-Kirchoff theorem from optics is used to calculate the atomic image $U(\underline{r})$ (actually the source wavefield) from:

$$U(x,y,z) \propto \left| \iint_S \chi(\underline{k}) \exp[i\underline{k}\cdot\underline{r}] d\sigma_k \right| , \quad (10)$$

where the integral on the direction of $\underline{k}$ is over the spherical surface on which the hologram is measured. Note that $\chi(\underline{k})$ has here been multiplied by the complex conjugate of the direction-dependent part of the phase factor due to path length difference $\exp[-i\underline{k}\cdot\underline{r}]$, and that the magnitude of $\underline{k}$ is fixed. Applying Eq. 10 to $\chi(\underline{k})$ as written in Eq. 6 them immediately predicts the existence of both real and twin images at $\pm\underline{r}_j$, as well as weaker self-interference images at $\pm(\underline{r}_j - \underline{r}_k)$, both potentially complicating features in structural studies. Self-interference effects have been predicted by Thevuthasan et al. [29b,34a] to be generally only $\leq$10-20% as strong as the real and twin images, although they may not always be negligible. Further taking the z axis to be along the symmetry axis of the hologram and thus usually also to be perpendicular to the surface and then projecting $\chi(\underline{k})$ onto the k_x-k_y surface plane (cf. Fig. 4) permits doing a two-dimensional Fourier transform with z as a variable parameter to yield the image U in a given z plane as [7a]:

$$U(x,y,z) \propto \left| \iint \{\chi(\underline{k})\exp[ik_z z]\} \cdot \exp[i(k_x x + k_y y)] dk_x dk_y \right| . \quad (11)$$

If the full opening angle of the hologram as centered on the z-axis normal to the surface is defined to be α, it can further be shown [7a,7b] that the uncertainties with which positions can be determined in the three coordinates are given by: $\Delta x = \Delta y = 1.22\pi/[k\sin(\alpha/2)] = 0.61\lambda_e/\sin(\alpha/2)$ in the surface plane and $\Delta z \simeq 4\pi/[k\sin^2(\alpha/2)] = 2\lambda_e/\sin^2(\alpha/2)$ perpendicular to the surface plane, where λ_e is the electron de Broglie wavelength. These uncertainties can also be inversely related via the Uncertainty Principle to the ranges Δk_x, Δk_y, and Δk_z that are spanned by the hologram [28b,35]: $\Delta x \simeq 1/\Delta k_x$, $\Delta y \simeq 1/\Delta k_y$, and $\Delta z \simeq 1/\Delta k_z$.

Holographic images also may be distorted due to anisotropy in the amplitudes of both the reference wave ϕ_o and the scattered waves ϕ_j, as well as the often significant phase shifts Ψ_j due to scattering. Possible solutions to these problems are to eliminate or correct regions of the hologram that are most non-ideal, as for example, over the forward scattering peaks [28,34a].

To further improve atomic image positions, it is necessary to somehow correct for anisotropic scattering amplitudes and/or phase shifts in doing the image-producing transform [36]. One correction method proposed by Tonner, Saldin and co-workers [36a] is simply to normalize $\chi(\underline{k})$ by a generalized scattered-wave strength F_j during the integration, which yields a new image function U':

$$U'(x,y,z) \propto \left| \iint \{\chi(\underline{k})\exp[ik_z z]/F_j(\underline{k},\underline{r})\} \cdot \exp[i(k_x x + k_y y)] dk_x dk_y \right| . \quad (12)$$

This has been termed the

scattered-wave-included Fourier transform (SWIFT) method. In practice, this procedure has to date generally involved simply dividing by a plane-wave or spherical-wave scattering factor, which may then have to be adjusted with position in space so as to allow for the different types of scatterers present [29a-c,36]. The latter adjustment thus requires some advance knowledge of the structure, or an iterative approach. F_j also can in principle allow for the anisotropy in the outgoing reference wave, as is implicit in the factor $\hat{e}\cdot\hat{r}_j$ in Eq. 3c; this more general type of correction has been applied for the first time to experimental data from $CoSi_2$(111) by Zhou et al. [30].

We illustrate some of these principles for the well-known test case of c(2x2)S on Ni(001), as studied by Thevuthasan et al. [29b,c]. In Fig. 6 are shown experimental and theoretical holograms for S 2p emission from this overlayer at 1324 eV. Data were obtained only over the range of angles from 10° to 40° above the surface for which multiple scattering effects (strongest along the surface) are negligible and sufficient diffraction anisotropy exists to be conveniently measured in a conventional XPS system. The experimental data agree with theory in showing higher-order diffraction maxima (holographic fringes) that are associated with the nearest-neighbor (N-N) and next-nearest-neighbor (N-N-N) S atoms along the surface, centered at ϕ = 0° and 45°, respectively. Osterwalder et al. have seen similar holographic fringes in a study of c(2x2)Na on Al(001) [33].

Fig. 7 now shows experimental and theoretical atomic images based on the holograms of Fig. 6. in two different symmetry planes, as shown in the overlaid atomic geometries. A scattered-wave correction has been applied in forming the images according to Eq. 12. The images of the N-N sulfur atoms are clear in both experiment and theory, and there is good agreement as to the degree of shift relative to the true positions of about 0.3 Å. N-N-N sulfur atoms are seen in theory, but not experiment, probably due to the noise level in the data. The underlying Ni atoms are not seen in either experiment or theory, due to both weaker back scattering and stronger Debye-Waller effects at this higher kinetic energy. Similar N-N adsorbate images have been found with a Fourier-transform analysis of Na 1s emission at a lower energy of 182 eV from c(2x2)Na on Al(001) by Osterwalder and co-workers [33]. Other single-energy, SWIFT-corrected results for bulk $CoSi_2$ at 700 eV are also encouraging [30].

The overlap of real and twin images is a problem shared with optical holography, but it is potentially more serious in images of surface structures, since the surface inherently breaks the inversion symmetry along its normal, and thus the twins of substrate atoms may overlap the regions in space occupied by adsorbate or overlayer atoms. One solution to this problem is to note that, for some cases, the region of the hologram most strongly affected by some atom at $\underline{r}$ is well localized in a solid-angle region centered on $\underline{r}$; this

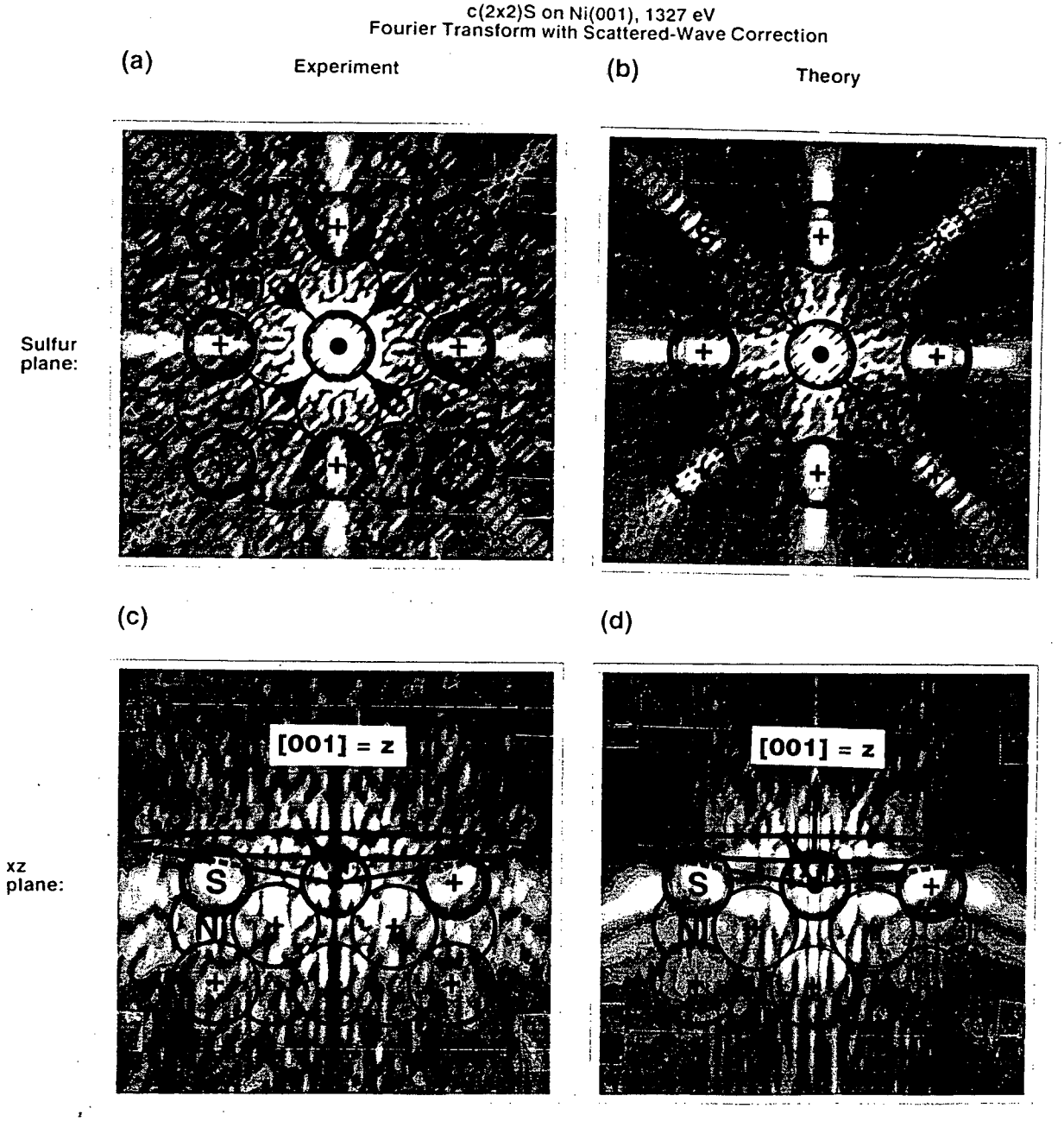

Fig. 7- Fourier-transform holographic images for c(2x2)S/Ni(001) based on the holograms of Fig. 6. A scattered-wave correction according to Eq. 12 has been used. Images are shown in both the sulfur (=xy) and xz planes. Results are shown for both experiment ((a) and (c)) and single-scattering theory ((b) and (d)). The known atomic positions are indicated by the overlays. [From Thevuthasan et al. ref. 29c]

was first demonstrated in theoretical simulations by Saldin et al. [37]. Analyzing only this portion of the hologram then may lead to an image in which the twin from another atom at $-\underline{r}$ is suppressed, as suggested by Saiki et al. for scanned-angle data from cases dominated by forward scattering [38], and used successfully by Thevuthasan et al. [29b,c] in analyzing S/Ni. For back-scattering cases at lower energies, Tong et al. [36b] have also proposed analyzing scanned-energy data over only small windows in direction in order to emphasize a single scatterer behind the emitter.

The work to date thus suggests that even single-energy holographic images for adsorbate overlayers or thin epitaxial layers can be obtained with sufficient accuracy to be used for ruling out many possible structures and providing excellent starting points for more accurate final trial-and-error refinements. However, previous studies on multilayer bulk specimens of Cu [28a], Ni [22], Si [29a] and Ge [23b] at higher single energies suggest that the presence of inequivalent emitters in several layers can lead to strong image distortions along forward scattering directions.

A more general approach for suppressing twins, as well as other deleterious effects in images, has also been suggested by Barton [7c], and it involves making phased summations of transforms of scanned-angle data obtained at different energies E_i with wave vectors $\underline{k}_i$ according to:

$$U''(x,y,z) \propto \left|\Sigma_i \exp[-ik_i r] \cdot \iint_S \chi(\underline{k}_i)/\exp[i\underline{k}_i\cdot\underline{r}]d\sigma_k\right| \tag{13a}$$

$$\propto \left|\Sigma_i \exp[-ik_i r] \cdot \iint \{\chi(\underline{k}_i)\exp[ik_{iz}z]/F_j(\underline{k}_i,\underline{r})\} \cdot\exp[i(k_{ix}x + k_{iy}y)]dk_x dk_y\right| . \tag{13b}$$

This sum can in principle be performed either with or without correction for the outgoing and scattered waves, although it has been included above in dividing again by $F_j(\underline{k},\underline{r})$ in Eq. 13b. In doing this sum, we have multiplied by the conjugate of the remaining phase factor due to path length difference exp[ikr], with $\chi(\underline{k})$ containing such factors inside of the F_j's (cf. Eqs. 2 and 3). The sum on k_i now varies the magnitude of $\underline{k}$, and selects out peaks at r_j in space for which $\chi(\underline{k})$, through the F_j's, contains phase factors $\exp[ikr_j]$. This method has been demonstrated to suppress twin images [7c,29b,c,35], most multiple scattering effects [7c], and self-interference effects [34b]. For example, encouraging experimental images have been obtained for inherently more difficult bulk samples of Cu(001) by Terminello et al. [31a] and of Pt(111) by Petersen et al. [31b].

As an illustration of how well images can be improved by this summed-energy approach, we show in Fig. 8 a theoretical simulation of images for the same c(2x2)S/Ni(001) system [34b]. The sum was over 13 energies between 862 and 1324 eV, with a constant δk step of 0.3 $Å^{-1}$. The hologram was here calculated over the region from 30° above the surface to normal, which should be the most nearly ideal portion of it,

c(2x2)S on Ni(001), 13 energies, 862-1327 eV
Sum of Fourier Transforms, Theory

(a) Sulfur plane:

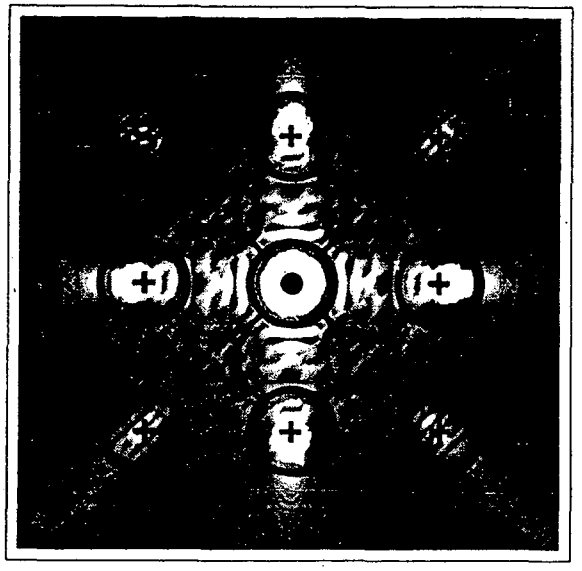

(b) xz plane:

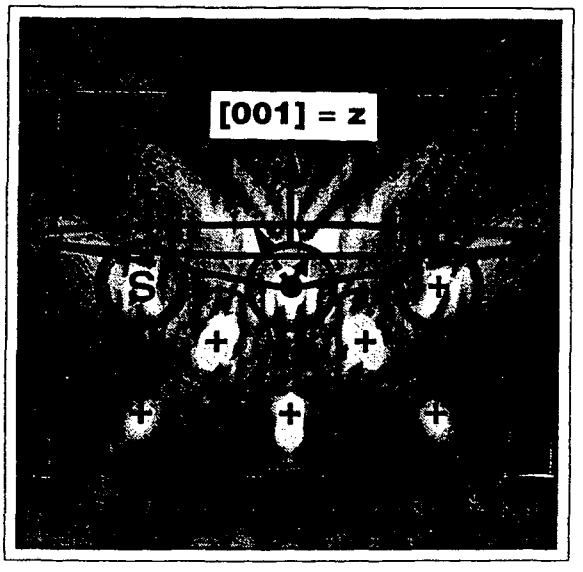

Fig. 8- Theoretical Fourier transform images in the sulfur and xz planes based on S 2p emission from c(2x2)S/Ni(001). A phased sum of transforms according to Eq. 13a has been made over 13 energies between 862 and 1324 eV. [From Thevuthasan et al., ref. 34b]

with weak, more isotropic, single scattering being dominant. Even with no scattered-wave corrections, the peak positions are here in excellent agreement with the known structure, the N-N and N-N-N S atoms are both visible, and the five Ni atoms underneath a typical S emitter are clearly seen. This simulation makes the use of such summed-energy analyses look extremely encouraging for adsorbate and thin overlayer structure studies, although the Ni atoms below the S emitter will probably be more weakly imaged in experiment due to the fact that no vibrational effects were included in these calculations.

An important question that immediately arises is how many energies need to be summed over, and how small the steps δk between them need to be to optimally reduce image aberrations and artifacts. It has been found in various theoretical simulations that about 10 energies spaced by a constant δk are sufficient to yield essentially complete twin and multiple scattering suppression [29b,34b,35]. In addition, the size of δk must be small enough to push artifacts (related to aliasing in standard Fourier transform theory) outside of the range of interatomic distances that are to be studied [7c,29b,35]. The behavior of these artifacts is illustrated in Fig. 9, where images in the sulfur plane of c(2x2)S/Ni(001) are shown for different numbers of energies spanning the range from 862 to 1324 eV. Only the right half of the hologram has here been analyzed to emphasize the real image due to the nearest-neighbor along +x. In going from 1 to 3 to

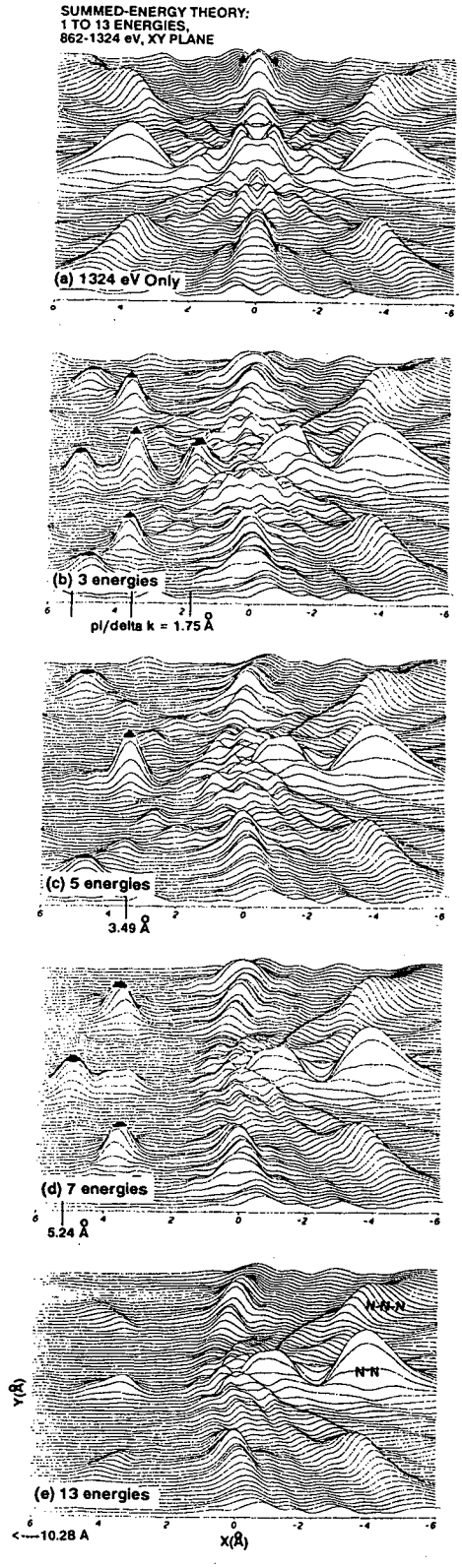

Fig. 9- Theoretical Fourier transform images for c(2x2)S/Ni(001) in the sulfur plane obtained using only the right half of a hologram extending from 10° to 50° above the surface. Data are shown for different numbers of energies in a phased sum according to Eq. 13b, but with no scattered-wave correction: (a) 1 energy, (b) = 3 energies, (c) = 5, (d) = 7, and (e) = 13. The multiples of $\pi/\delta k$ at which artifacts can remain on spherical surfaces surrounding the origin are also indicated; the shaded peaks all occur at such positions. [From Thevuthasan et al., ref. 34b]

5 to 7 to 13 energies, we see a gradual suppression of twin-related features in the left half of the image, as expected. But anomalous features remain in circles at multiples of $\pi/\delta k$ away from the origin and these are fully moved out of the region of interest only in the last panel with 13 energies. Thus, such criteria on the choice of δk are crucial if image artifacts are to be suppressed.

Tong and co-workers [39] have also proposed a similar holographic approach for analyzing scanned-energy data so as to simultaneously correct for scattered-wave anisotropies and eliminate twin and multiple-scattering effects. This method makes use of a number of scanned-energy diffraction curves that are then Fourier transformed, summed, and used to determine the real-image positions of certain atoms. What is done in this procedure is to Fourier transform a $\chi(\underline{k}_q)$ obtained along the direction k_q over small steps in k_q first and then to carry out a phased sum over several larger steps in direction, as shown below:

$$U''''(x,y,z) \propto \left|\Sigma_q \exp[i\underline{k}_q\cdot\underline{r}] \cdot \int_{\Delta k_q} \chi(\underline{k}_q)\exp[-ik_q r]dk_q\right| . \qquad (14)$$

Corrections for scattering amplitudes and/or phase shifts can also be included in this integral, in the same spirit as indicated in Eq. 13b. Encouraging atomic images have been obtained using this approach for ($\sqrt{3}$ x $\sqrt{3}$)Al on Si(111) by Wu et al. [32].

Comparison of Eqs. 13a and 14 makes it clear that the approaches of Barton and Tong are fundamentally equivalent, in that they just interchange the order of integration and summation, with the same overall phase factor of $\exp[-ikr]\exp[i\underline{k}\cdot\underline{r}] = \exp[-ikr(1-\cos\theta)]$. However, the first emphasizes finer steps in $\hat{k}$ and the other finer steps in k. Thus, if both are carried out over equivalent ranges of Δk_x, Δk_y, and Δk_z, one would expect corresponding resolutions in the coordinates x, y, and z, provided that the $\underline{k}$ steps are sufficiently small in all directions to avoid spurious features due to the non-cancellation of twin and multiple scattering features (cf. Fig. 9). If applied correctly, both methods should be equally capable of suppressing twin and multiple scattering effects. For a given image accuracy and scope in $\underline{r}$ space, it is also expected that these two approaches would require about the same size of data set: something like 3,000-5,000 intensities with allowance for surface symmetry.

In fact, these two methods of summing/integrating over intensities are really just the two limits of a continuous range of choices in sampling a given volume of $\underline{k}$ space, as illustrated in Fig. 10 [40]. Here are shown the holographic images for a simple pyramidal cluster of Cu atoms as computed according to Eq. 13 (or equivalently Eq. 14), with no scattered-wave corrections. The sampling of $\underline{k}$ space has been varied so as to change from fine steps in direction and course steps in energy ("scanned-angle" data) to course steps in direction and fine steps in energy ("scanned-energy" data). However, the total number of data points has been kept constant at about

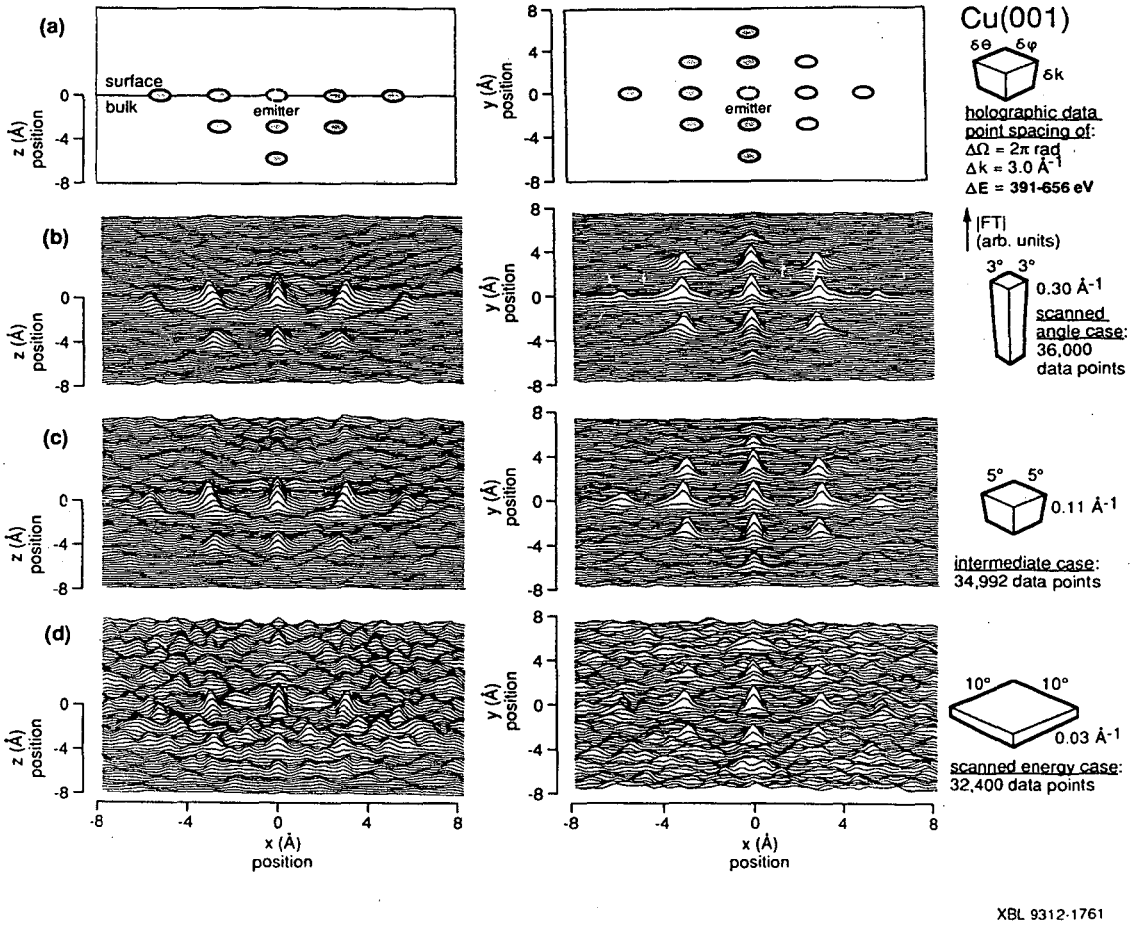

Fig. 10- Multi-energy theoretical holographic images derived from Eq. 13 (or equivalently Eq. 14) with no scattered-wave correction for a single emitter in the center of a pyramidal Cu cluster simulating the (001) surface. Full 2π holograms have been calculated and the total ranges in $\underline{k}$ and E considered have been kept constant at 3.0 $Å^{-1}$ and 391-656 eV, respectively. The total number of data points also has been held nearly constant, but the sampling of $\underline{k}$ space is varied from (b) = dense in direction ("scanned-angle") to (d) = dense in energy ("scanned-energy"). The sampling volume element is defined by $\delta\theta$ and $\delta\phi$ in degrees, and δk in $Å^{-1}$. The number of energies involved is 11 in (b), 28 in (c), and 101 in (d). [From Len et al., 40]

4,000-4,500 over the symmetry-reduced 1/8 of the hemisphere that would be necessary to study for this problem. It is clear that similar images can be obtained over a range of choices between scanned-angle and scanned-energy, but that going to too-widely-spaced choices in direction (panel (d)) or energy (cf. Fig. 9) can cause image deterioration. Thus, a variety of data taking options should be available in photoelectron holography.

Some advantages of the scanned-angle/summed-energy limit should be pointed out however: Scanning a monochromator (and perhaps also an undulator gap in next-generation synchrotron radiation experiments) is more difficult than scanning a specimen goniometer [1] or using a display analyzer [4c,31] to accumulate data over a broad range of solid angle at one time. Also, Auger electrons at fixed kinetic energy often interfere with measuring photoelectron intensities continuously over a sufficient range of energies, but this problem might be avoided by choosing suitable energy increments in a scanned-angle approach. In either the scanned-angle or scanned-energy approach, intensities have to be normalized for variations in photon flux with time and photoelectric cross sections with energy, as well as for any other purely instrumental effects on $\chi(\underline{k})$, but this procedure is probably somewhat simpler in the scanned-angle mode.

Finally, we comment on the extra amount of data required in photoelectron holography relative to more standard applications of photoelectron diffraction. It has been suggested that this additional effort is unnecessary, as methods based upon Eq. 8 can already be used to derive reasonably good first estimates of nearest-neighbor positions for subsequent trial-and-error structure determinations [24]. However, these simpler approaches do not have the potential of getting information on neighbors further away, whereas holography does [cf. Figs. 7-10 and refs. 30-32]. Also, some of these approaches [24] seem limited to emission from atomic or small-molecule adsorbates, but not to be suitable for buried species, e.g. in epitaxial overlayers. Finally, the net increase in data required appears to be only about 3-5x, a factor which should be tractable with higher-brightness synchrotron radiation sources.

PHOTOELECTRON DIFFRACTION WITH CIRCULARLY-POLARIZED RADIATION

If instead of linearly-polarized radiation, left or right circularly-polarized radiation is used for core-level excitation, two distinct kinds of circular dichroism (CD) can occur, as reviewed by Schönhense [15]: one due to emission in some sort of chiral experimental geometry (what we will call "normal" dichroism), and one due to spin-orbit splitting in the presence of an external magnetic field (magnetic CD or MCD). The latter is based on the well-known Fano effect first discussed for atoms: the selection rule $\Delta m_j = \pm 1$ for left or right polarized radiation can cause preferential excitation of spin-up or spin-down electrons, even if there were equal populations of the two types in the initial spin-orbit-split core

states. In either case, the degree of dichroic asymmetry can be measured as a function of $\underline{k}$ via

$$A^{CD}(\underline{k}) = [I^{RCP}(\underline{k}) - I^{LCP}(\underline{k})] / [I^{RCP}(\underline{k}) + I^{LCP}(\underline{k})] , \quad (15)$$

where I^{RCP} and I^{LCP} are the intensities measured with right and left polarized light, respectively. Very few measurements of the $\underline{k}$ dependence of A^{CD} in core-level emission have been made to date, but we illustrate the types of effects expected with two examples.

Bansmann and co-workers [41a] have studied normal CD in C 1s emission from CO adsorbed on Pd(111) in a chiral experimental geometry. Some of their experimental data as a function of a particular electron emission angle θ are shown in Fig. 11 together with theoretical calculations based on several models [41b,c]. The effects are quite pronounced, being as large as $\pm$75% variations in A^{CD}. The three theoretical curves all agree reasonably well with the data: two are based upon treating an isolated CO molecule only, and one includes the effect of the Pd substrate as a 19-atom cluster. Two of these curves (------ and · --- ·) have been calculated by Westphal et al. [41c] in a multiple-scattering diffraction picture of the outgoing wave, thus emphasizing the fact that it is only through photoelectron scattering and diffraction from neighboring atoms that normal circular dichroism can manifest itself in core-level emission. Diffraction theory including the effects of the underlying Pd atoms (· --- ·) shows that the substrate could produce additional fine structure on such data, but there are as yet no conclusive experimental data indicating such effects. The future measurement of circular dichroism in core emission with synchrotron radiation from insertion devices designed to produce high-brightness circularly-polarized radiation, coupled with analysis in terms of more accurate cluster-based multiple-scattering calculations [8b-d], thus represents a very interesting new direction of study in photoelectron diffraction.

MCD in core-level emission has so far been studied only for a few cases, and then only with a fixed emission direction. In Fig. 12, we show the first data of this type due to Baumgarten et al. [42a] for Fe $2p_{1/2,3,2}$ emission from Fe(110). In the lower part of (a) are shown two partial spectra obtained with the sample magnetization parallel to- and anti parallel to- the direction of helicity of circularly-polarized radiation; this is equivalent to changing from right to left polarization in the frame of the sample. The full spectrum in (a) represents an average over the two magnetizations. In (b), A^{CD} is plotted, and it is clear that significant effects of the order of a few percent are seen, even if they are much smaller than those found for normal CD in Fig. 11. Similar results have been obtained by Waddill et al. [42b] for Fe 2p emission from thin overlayers of Fe on Cu(001), again for a fixed direction of emission. Both sets of data have been qualitatively explained in terms of preferential excitation of photoelectrons of

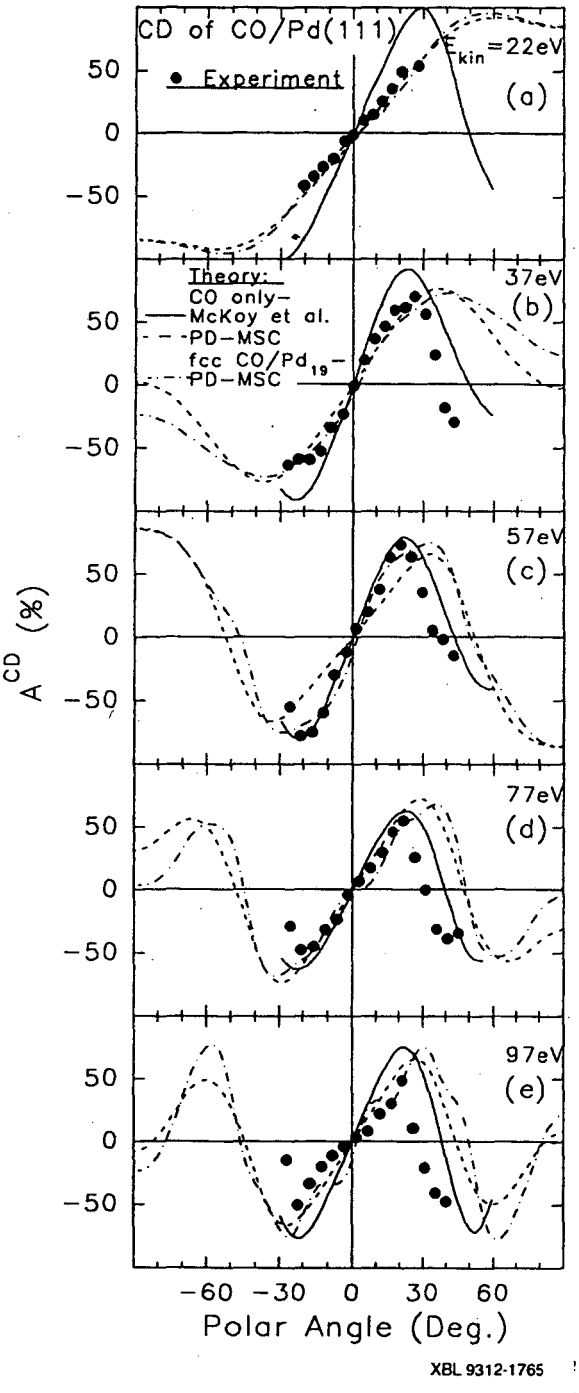

Fig. 11- Normal circular dichroism in C 1s emission from CO adsorbed on Pd(111). The experimental data are from Bansmann et al. [ref. 41a] and the solid theoretical curve from quantum-chemical calculations by McKoy et al. [ref. 41b]. The other two theoretical curves (------ = CO only and · --- · = CO in fcc sites on a 19-atom Pd(111) cluster, with the θ scan in the [10,-1] azimuth) are from Westphal et al. [ref. 41c] and are based upon multiple-scattering photoelectron diffraction calculations.

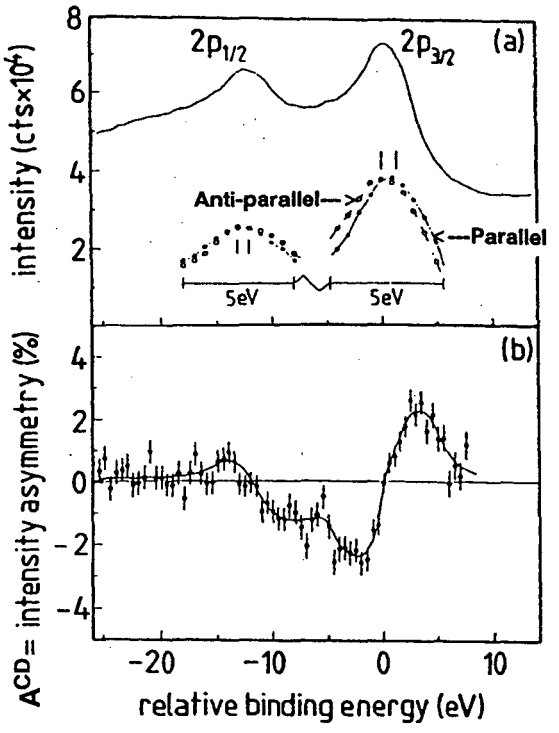

Fig. 12- Magnetic circular dichroism in Fe 2p emission from Fe(110). In (a), the average full spectrum is shown together with data for photon incidence parallel to- and anti-parallel to- the specimen magnetization. In (b), the asymmetry as calculated from Eq. 15 is plotted. [From Baumgarten et al., ref. 42a]

one spin or another in the $2p_{1/2}$ and $2p_{3/2}$ peaks, combined with a spin-dependent splitting in the core level that is probably linked to multiplet effects [42a]. However, the analysis of such MCD data has not yet included interference between the l_{final} = 0 and 2 photoelectron channels, nor has any spin-dependent final-state scattering and diffraction been considered. It is also clear that normal CD can co-exist with MCD, and that both types of effect in general need to be considered simultaneously [41a,c]. Thus, future studies in which both normal CD and MCD are measured over a range of $\underline{k}$ and analyzed more precisely with inclusion of both of these effects represent an important area of future development in photoelectron diffraction.

PHOTOELECTRON DIFFRACTION AND HOLOGRAPHY WITH SPIN RESOLUTION

If the spin of an outgoing photoelectron can somehow be determined, either through its origin in a well-defined multiplet splitting [14a] or through direct external measurement with respect to an external magnetization axis [16], then the spin-dependent aspects of photoelectron diffraction can be studied, for example, by comparing the patterns produced by exiting spin-up and spin-down electrons. These effects were first studied by Sinkovic et al. [14b], who made use of multiplet-split levels to provide the spin resolution. Experimental data from these studies [14b-d] provided evidence for a high-temperature loss of surface short-range antiferromagnetic order that had not been observed previously. Some results from a study on antiferromagnetic MnO(001) [14d] are shown in Fig. 13(a). In Fig. 13(a)(i), with a low kinetic energy of 111 eV for which magnetic scattering effects are more pronounced [14b], a sharp change in the spin-up/spin-down intensity ratio is found at a temperature of 530K that is about 4.5 times the bulk antiferromagnetic-to-paramagnetic transition temperature (Neél temperature). At a higher kinetic energy of 1405 eV in Fig. 13(a)(ii) for which magnetic effects are expected to be negligible [14b], no such effects are seen.

Although the precise origin of this change in short-range magnetic order is not yet known, recent Monte Carlo calculations of spin-spin correlation functions on such antiferromagnetic surfaces by Zhang et al. [43] suggest that these measurements were in fact observing a surface Neél temperature several times that of the bulk. Some of these theoretical results are shown in Fig. 13(b), where a clear surface magnetic phase transition can be distinguished from the bulk transition for the particular choice of a surface magnetic coupling strength that is 6 times that in the bulk. In fact, the surface transition is distinct for any coupling strength greater than about 3 times that in the bulk. Beyond providing a new method for studying short-range magnetic order and magnetic phase transitions near surfaces, such spin-dependent photoelectron scattering and diffraction will also clearly be an important part of the analysis of MCD data such as that described in the last

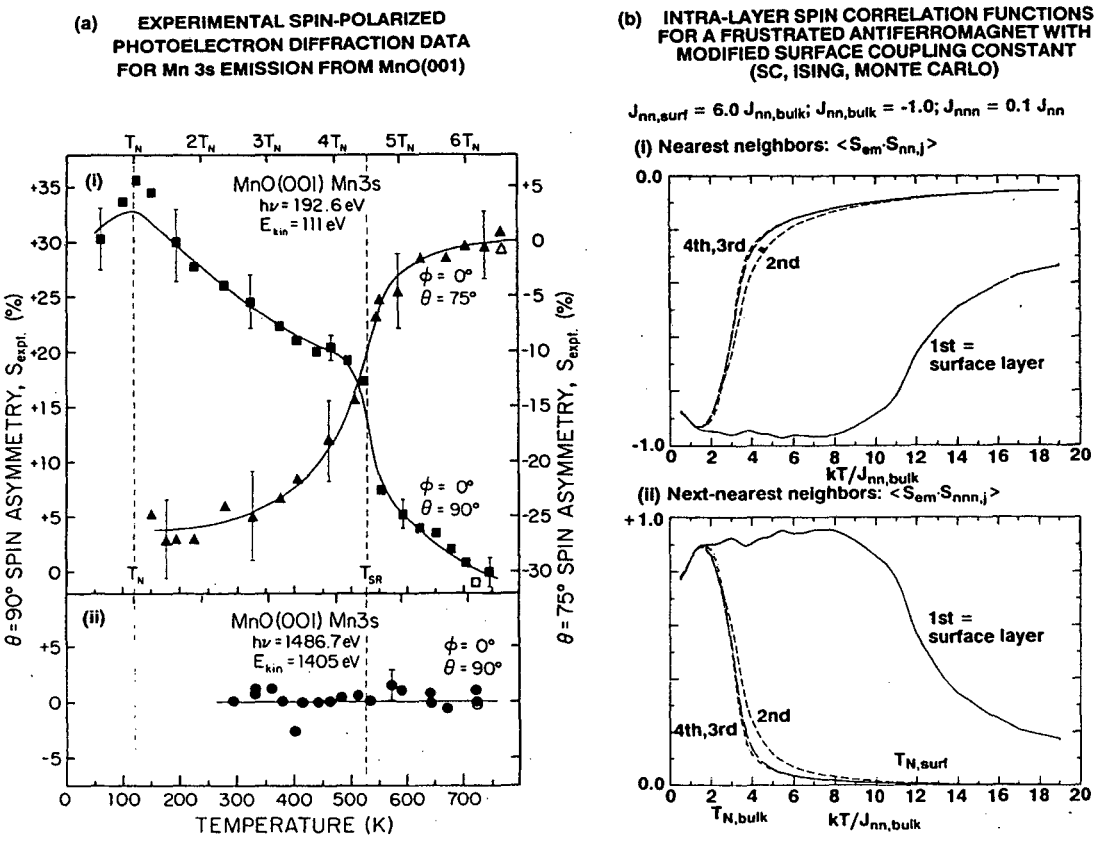

Fig. 13- (a) Experimental spin-polarized photoelectron diffraction results for 3s emission from MnO(001). The spin-up/spin-down ratio, as measured by an asymmetry parameter $S_{expt.}$, exhibits an abrupt change in value at about 530K (about 4.5 times the bulk transition temperature) with a low photoelectron kinetic energy of 111 eV, but no change with an energy of 1405 eV. [From Hermsmeier et al., ref. 14d] (b) Theoretical spin-spin correlation functions between a Mn emitter and its neighbors in a simulated MnO lattice as a function of temperature, as derived from Monte Carlo calculations. For a surface intralayer coupling strength that is 6 times the value in the bulk, a surface antiferromagnetic-to-paramagnetic transition occurs at about 4 times the bulk transition temperature. [From Zhang et al., ref. 43]

section.

In two recent studies the additional possibility of spin-polarized photoelectron holography has been considered [44]. Although there is as yet no experimental data on this subject, Kaduwela et al. [44a] have carried out model calculations on simple clusters. Some of these results are shown in Fig. 14 for a two-atom cluster in which one Mn^{2+} ion is the emitter and the other is a magnetically-ordered scatterer. In order to look for spin-dependent exchange effects in the scattering, Fourier-transform images U(x,y,z) were first calculated from Eq. 11 in a plane containing the axis of the cluster for outgoing spin-up and spin-down electrons; no scattered-wave correction was used in order to focus on the spin-dependent differences in the images. The kinetic energy was held constant at a low value of 120 eV for both cases to insure strong magnetic scattering effects. An exchange interaction with the five parallel-coupled 3d electrons was included in the scattering potential if the photoelectron spin was parallel to the net spin of the Mn^{2+} scatterer (↑,↑ or ↓,↓), and was omitted if the photoelectron spin was antiparallel to the scatterer spin (↑,↓ or ↓,↑). The two simplest measures of these exchange effects in holographic images are:

$$\Delta(x,y,z,\uparrow-\downarrow,\uparrow) = U(x,y,z,\uparrow,\uparrow) - U(x,y,z,\downarrow,\uparrow), \quad (16)$$

which is simply a difference of two normal images, and

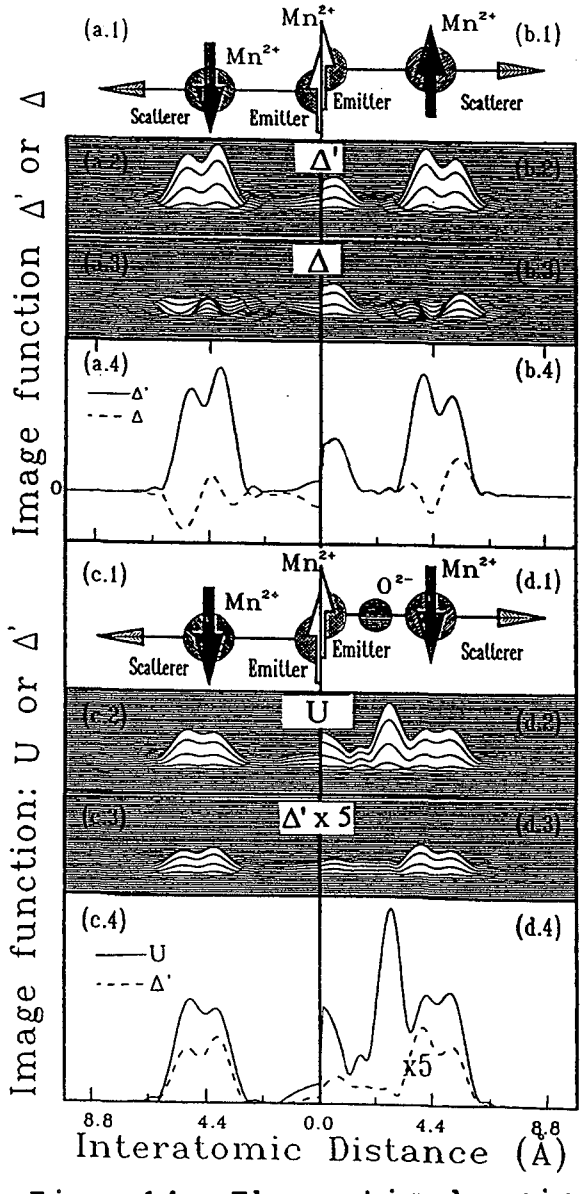

Fig. 14- Theoretical spin-polarized holographic images at 120 eV based upon the (spin-up) - (spin-down) difference functions Δ (Eq. 16) and Δ' (Eq. 17) for a cluster of Mn^{2+} ions consisting of an emitter and scatterer that are 4.4 Å apart ((a.1)-(b.4)). In (c.1)-d.4), the effect of including a non-magnetic O^{2-} scatterer on the image function U and on Δ' are illustrated. [From Kaduwela et al., ref. 44a]

$$\Delta'(x,y,z,\uparrow-\downarrow,\uparrow) =$$

$$\left|F_\sigma(x,y,z,\uparrow,\uparrow) - F_\sigma(x,y,z,\downarrow,\uparrow)\right|, \quad (17)$$

in which F_σ is the (complex) Fourier transform integral within U and the absolute value is taken after calculating the difference. The second spin argument here is the orientation of the scatterer, here chosen to be up. Through its sign, Δ can be shown to be sensitive to the orientation of the scatterer, whereas the always-positive Δ' can be shown to measure more directly the strength of the spin-dependent exchange scattering.

In Fig. 14, the image functions Δ and Δ' are plotted for the two different orientations of the scatterer: spin-down in parts (a.2)-(a.4) and spin-up in parts (b.2)-(b.4). The effects seen here are 10-15% of the magnitude of the peaks in the direct U images, and thus should be measurable, especially from higher-quality experimental data obtained with a next-generation synchrotron radiation source. As expected from their definitions, Δ and Δ' exhibit different behavior on flipping the scatterer spin: Δ changes in sign, whereas Δ' does not. Thus, it has been suggested that the locations of near-neighbor magnetic scatterers could be determined via Δ', and actual spin flips (e.g., as temperature is changed) could be detected via Δ [44]. In parts (c.1)-(c.4) and (d.1)-(d.4), the effect of adding a non-magnetic O^{2-} scatterer midway between the two Mn^{2+} ions, with the scatterer spin being down, is considered. Although the normal image function U shows a strong additional peak due to the non-magnetic scatterer, this peak is strongly suppressed in Δ', verifying that the latter should be useful for imaging only the magnetic scatterers in a system.

REFERENCES

+ Work supported by the U.S. Department of Energy, Basic Energy Sciences, Materials Science Division, under Contract DOE-AC03-76SF00098, and the Office of Naval Research, under Contracts N00014-90-J-1457 and N00014-92-J-1140.

[1] (a) C.S. Fadley, Phys. Scripta T17 (1987) 39 ; (b) C.S. Fadley in Synchrotron Radiation Research: Advances in Surface Science, edited by R.Z. Bachrach (Plenum, New York, 1993); (c) C.S. Fadley, Surf. Sci. Repts., December, 1993; (d) C.S. Fadley, Mat. Res. Soc. Symp. Proc. 307 (1993) 261 ; (e) R.S. Saiki, A.P. Kaduwela, J. Osterwalder, D.J. Friedman, C.S. Fadley, and C.R. Brundle, Surf. Sci. 281 (1993) 270 .

[2] (a) S.A. Chambers, Adv. in Phys. 40 (1990) 357 ; S.A. Chambers, Surf. Sci. Repts. 16 (1992) 261 ; (b) W.F. Egelhoff, Jr. in Critical Reviews in Solid State and Materials Sciences, 16 (1990) 213 ; (c) D. Naumovic, A. Stuck, T. Greber, J. Osterwalder, and L. Schlapbach, Phys. Rev B. 47 (1993) 7462 ; A. Fischer, R. Fasel, J. Osterwalder, A. Krozer, and L. Schlapbach, Phys. Rev. Lett. 70 (1993) 1493 .

[3] H.P. Bonzel, Prog. in Surf. Sci. 42 (1993) 219.

[4] (a) L.J. Terminello, X.S. Zhang, Z.Q. Huang, S. Kim, A.E. Schach von Wittenau, K.T. Leung,

and D.A. Shirley, Phys. Rev. B38(1988) 3879; (b) L.-Q. Wang, Z. Hussain, Z.Q. Huang, A.E. Schach von Wittenau, D.A. Shirley, and D.W. Lindle, Phys. Rev. B44 (1991) 13771 ; (c) D.A. Shirley, Y. Zheng, B.L. Petersen, Z. Hussain, W.A. Huff, J.J. Barton, and L. Terminello, paper in these Proceedings.

[5] A.M. Bradshaw and D.P. Woodruff, Applications of Synchrotron Radiation: High-Resolution Studies of Molecules and Molecular Adsorbates on Surfaces, edited by W. Eberhardt (Springer-Verlag, Berlin, 1993), in press.

[6] A. Szöke, in Short Wavelength Coherent Radiation: Generation and Applications, edited by D.T. Attwood and J. Bokor, AIP Conference Proceedings No. 147 (AIP, New York, 1986).

[7] (a) J.J. Barton, Phys. Rev. Lett. 61 (1988) 1356; (b) J.J. Barton, J. Electron Spectrosc. 51 (1990) 37 ; (c) J.J. Barton, Phys. Rev. Lett. 67 (1991) 3106.

[8] (a) C.H. Li and S.Y. Tong, Phys. Rev. Lett. 42 (1979) 901; (b) J.J. Barton and D.A. Shirley, Phys. Rev. B32 (1985) 1892 and 1906; (c) A.P. Kaduwela, G.S. Herman, D.J. Friedman and C.S. Fadley, Phys. Scripta 41 (1990) 948; (d) A.P. Kaduwela, D.J. Friedman, and C.S. Fadley, J. Electron Spectrosc. 57 (1991) 223 ; (e) A.P. Kaduwela, M.A. Van Hove, and C.S. Fadley, unpublished results.

[9] D.J. Friedman and C.S. Fadley, J. Electron Spectrosc. 51 (1990) 689.

[10] (a) P.J. Orders and C.S. Fadley, Phys. Rev. B27 (1983) 781; (b) M. Sagurton, E.L. Bullock, and C.S. Fadley, Phys. Rev. 30 (1984) 7332 .

[11] J. Osterwalder, T. Greber, S. Hüfner, and L. Schlapbach, Phys. Rev. B41 (1990) 12495; S. Hüfner, J. Osterwalder, T. Greber, and L. Schlapbach, Phys. Rev. B42 (1990) 7350 ; G.S. Herman and C.S. Fadley, Phys. Rev. B43 (1991) 6792 ; T. Greber, J. Osterwalder, S. Hüfner, and L. Schlapbach, Phys. Rev. B44 (1991) 8958.

[12] G. Waddill, J.G. Tobin, H. Li, and S.Y. Tong, Phys. Rev. Lett. 70 (1993) 4150 .

[13] (a) D. Sebilleau, M.C. Desjonqueres, D. Chaveau, C. Guillot, J. Lecante, G. Treglia, and D. Spanjaard, Surf. Sci. Lett. 185 (1987) L527; (b) A. Nilsson, H. Tillborg, and N. Mårtensson, Phys. Rev. Lett. 67 (1991) 1015; (c) K.U. Weiss et al., Phys. Rev. Lett. 69 (1992) 3196; (d) J.D. Denlinger, E. Rotenberg, U. Hessinger, M. Leskovar, and M.A. Olmstead, Appl. Phys. Lett. 62 (1993) 2057, and E. Rotenberg, J.D. Denlinger, U. Hessinger, M. Leskovar, and M.A. Olmstead, J. Vac. Sci. Tech. B11 (1993) 1444.

[14] (a) C.S. Fadley and D.A. Shirley, Phys. Rev. A2 (1970) 1109; (b) B. Sinkovic, B.D. Hermsmeier, and C.S. Fadley, Phys. Rev. Lett. 55 (1985) 1227; (c) B.D. Hermsmeier, J. Osterwalder, D.J. Friedman, and C.S. Fadley, Phys. Rev. Lett. 62 (1989) 478; (d) B.D. Hermsmeier, J. Osterwalder, D.J. Friedman, B. Sinkovic, T.T. Tran, and C.S. Fadley, Phys. Rev. B42 (1990) 11895; (e) B. Sinkovic, D.J.

Friedman, and C.S. Fadley, J. Magn. Magn. Mater. 92 (1991) 301.

[15] G. Schönhense, Physica Scripta T31 (1990) 255.

[16] F.U. Hillebrecht, R. Jungblut, and E. Kisker, Phys. Rev. Lett. 65 (1990) 2450; R. Jungblut, Ch. Roth, F.U. Hillebrecht, and E. Kisker, J. Appl. Phys. 70 (1991) 5923; R. Jungblut, Ch. Roth, F.U. Hillebrecht, and E. Kisker, Surf. Sci. 269/270 (1992) 615; T. Kachel, C. Carbone, and W. Gudat, Phys. Rev. B47 (1993) 15391.

[17] S. Mroz and A. Mroz, Surf. Sci. 224 (1989) 235; S. Mroz and M. Nowicki, paper in these Proceedings; S. Valeri and A. Di Bona, Rev. del Nuovo Cimento 16 (1993) 1, and references therein.

[18] G.R. Harp, D.K. Saldin, and B.P. Tonner, Phys. Rev. Lett. 65 (1990) 1012; C.M. Wei, I.H. Hong, P.R. Jeng, S.C. Shyu, and Y.C. Chou, private communication.

[19] D.K. Saldin and P.L. de Andres, Phys. Rev. Lett. 65 (1990) 1012; and K. Heinz, U. Starke, and F. Bothe, Surf. Sci. Lett. 243 (1991) 670 .

[20] S. Thevuthasan, F. Zhang, R.X. Ynzunza, E.D. Tober, and C.S. Fadley, unpublished results.

[21] T. Hertel, T. Greber, and J. Osterwalder, unpublished results; S.D. Ruebush, R. Couch, H. Xiao, Z. Wang, S. Thevuthasan, and C.S. Fadley, unpublished results.

[22] O.M. Kuettel and J. Osterwalder, unpublished results.

[23] (a) U. Breuer, O. Knauff, and H.P. Bonzel, J. Vac. Sci. Tech. A8 (1990) 2489; U. Breuer, H.P. Bonzel, K.C. Prince, and R. Lipowsky, Surf. Sci. 223 (1989) 258; (b) T.T. Tran, S. Thevuthasan, Y.J. Kim, G.S. Herman, D.J. Friedman, and C.S. Fadley, Phys. Rev. B45 (1992) 12106; T.T. Tran, S. Thevuthasan, Y.J. Kim, D.J. Friedman, A.P. Kaduwela, G.S. Herman, and C.S. Fadley, Surf. Sci. 281 (1993) 270.

[24] (a) V. Fritzsche and D.P. Woodruff, Phys. Rev. B46 (1992) 16128; (b) P. Hofmann and K.M. Schindler, Phys. Rev. B 47 (1993) 13942.

[25] H.C. Poon and S.Y. Tong, Phys. Rev. B30 (1984) 6211; S.Y. Tong, H.C. Poon, and D.R. Snider, Phys. Rev. B32 (1985) 2096.

[26] R.X. Ynzunza, R. Couch, S. Ruebush, S. Chamberlain, S. Thevuthasan, A.P. Kaduwela, M.A. Van Hove, and C.S. Fadley, to be published.

[27] B.P. Tonner, Z.-L. Han, G.R. Harp, and D.K. Saldin, Phys. Rev. B43 (1991) 14423.

[28] (a) G.R. Harp, D.K. Saldin, and B.P. Tonner, Phys. Rev. Lett. 65 (1990) 1012; (b) G.R. Harp, D.K. Saldin, and B.P. Tonner, Phys. Rev. B42 (1990) 9199.

[29] (a) G.S. Herman, S. Thevuthasan, T.T. Tran, Y.J. Kim, and C.S. Fadley, Phys. Rev. Lett. 68 (1992) 650; (b) S. Thevuthasan, G.S. Herman, A.P. Kaduwela, T.T. Tran, Y.J. Kim, R.S. Saiki, and C.S. Fadley, J. Vac. Sci. Technol. A10 (1992) 2261; (c) S. Thevuthasan, R.X. Ynzunza, E.D. Tober, C.S. Fadley, A.P. Kaduwela,

and M.A. van Hove, Phy. Rev. Lett. 70 (1993) 595.

[30] Y. Zhou, X. Chen, J.C. Campuzano, G. Jennings, H. Ding, and D.K. Saldin, Mat. Res. Soc. Symp. Proc. 307 (1993) 279.

[31] (a) L.J. Terminello, J.J. Barton, and D.A. Lapiano-Smith, J. Vac. Sci. Technol. B10 (1992) 2088 and Phys. Rev. Lett. 70 (1993) 599. (b) B.L. Petersen, L.J. Terminello, and D.A. Shirley, Mat. Res. Soc. Symp. Proc. 307 (1993) 285, and private communication.

[32] H. Wu, G.J. Lapeyre, H. Huang, and S.Y. Tong, Phys. Rev. Lett. 71 (1993) 251.

[33] J. Osterwalder, R. Fasel, A. Stuck, P. Aebi, L. Schlapbach, paper in these Proceedings.

[34] (a) S. Thevuthasan, G.S. Herman, A.P. Kaduwela, R.S. Saiki, Y.J. Kim, W. Niemczura, M. Burger and C.S. Fadley, Phys. Rev. Lett. 67 (1991) 469 (b) S. Thevuthasan, P.M. Len, and C.S. Fadley, to be published.

[35] G.R. Harp, D.K. Saldin, X. Chen, Z.L. Han, and B.P. Tonner, J. Electron Spectrosc. 258 (1991) 313.

[36] D.K. Saldin, G.R. Harp, and B.P. Tonner, Phys. Rev. B45 (1992) 9629; (b) S.Y. Tong, C.M. Wei, T.C. Zhao, H. Huang, and H. Li, Phys. Rev. Lett. 66 (1991) 60.

[37] D.K. Saldin, G.R. Harp, B.L. Chen and B.P. Tonner, Phys. Rev. B44 (1992) 2480.

[38] R.S. Saiki, A.P. Kaduwela, J. Osterwalder, D.J. Friedman, C.S. Fadley, and C.R. Brundle, Surf. Sci. 279 (1992) 305.

[39] S.Y. Tong, H. Li, and H. Huang, Phys. Rev. Lett. 67 (1992) 3102; S.Y. Tong, H. Huang, and C.M. Wei, Phys. Rev. B46 (1992) 2452.

[40] P.M. Len, S. Thevuthasan, and C.S. Fadley, unpublished results.

[41] (a) J. Bansmann, Ch. Ostertag, G. Schönhense, F. Fegel, C. Westphal, M. Getzlaff, F. Schafers, and H. Petersen, Phys. Rev. B46 (1992) 13496; (b) V. McKoy, private communication; (c) C. Westphal, A.P. Kaduwela, M.A. Van Hove, and C.S. Fadley, to be published.

[42] (a) G. Baumgarten, C.M. Schneider, H. Petersen, F. Schafers, and J. Kirschner, Phys. Rev. Lett. 65 (1990) 492; (b) G.D. Waddill, J. Tobin, and D.R. Pappas, Phys. Rev. B46 (1992) 552.

[43] F. Zhang, S. Thevuthasan, R. Scalettar, R. Singh, and C.S. Fadley, to be published.

[44] (a) A.P. Kaduwela, Z. Wang, M.A. Van Hove, and C.S. Fadley, to be published; (b) E.M.E. Timmermans, G.T. Trammell, and J.P. Hannon, J. Appl. Phys. 73 (1993) 6183.

LAWRENCE BERKELEY LABORATORY
UNIVERSITY OF CALIFORNIA
TECHNICAL INFORMATION DEPARTMENT
BERKELEY, CALIFORNIA 94720